doi:10.20944/preprints202105.0562.v1

Active and stable $MgAl_2O_4$ and Ni(SA)/$MgAl_2O_4$ catalysts for the reverse water gas shift reaction

Lingling Zhang[1], Qi Song[2], Yimeng Xing[1], Zhichun Si[1], Yuxiang Liu[1,2], Rui Ran[2], Xiaodong Wu[1,2], Duan Weng[1,2], Feiyu Kang[1,2]*

1. Shenzhen International Graduate School, Tsinghua University, Shenzhen 518055, China
2. The Key Laboratory of Advanced Materials of Ministry of Education, School of Materials, Tsinghua University, Beijing 100084, China

Keywords: $MgAl_2O_4$, Single atomic Ni^{n+}, RWGS, Stability, Reaction mechanism

Abstract

Reverse water gas shift reaction (RWGS) is an important process which plays a vital role in many CO_2 utilization related reactions. Noble metals are the most active catalysts in RWGS, but the high price and low reserve strangled their applications. In the present work, we reported a non-transition-metal $MgAl_2O_4$ catalyst which showed outstanding activity and stability at high temperatures in the RWGS reaction and improved performance after doping of single atomic Ni^{n+}. The catalyst can obtain 46% of CO_2 conversion in durability test of 75 h at 800 °C under high weight hourly space velocities (225 000 ml g^{-1} h^{-1}). The adsorption sites, possible reaction route, and effects of Ni^{n+} single atoms on the (111) surface of $MgAl_2O_4$ for RWGS were investigated by in situ DRIFTS and DFT calculations. The results indicated that the rate determining reaction step of RWGS on $MgAl_2O_4$ and Ni (SA)/$MgAl_2O_4$ were both the reaction of $OH^* + H^* \rightarrow H_2O^* + {}^*$, but the energy barrier was significantly reduced after introducing single atomic Ni^{n+}. Ni^{n+} atoms can increase the hydroxyl coverage on the surface of catalyst and Al^{3+} sites near the Ni^{n+} ion are considered as the predominant active sites

---

[1] Corresponding author. Zhichun Si (Dr.), email: si.zhichun@sz.tsinghua.edu.cn

doi:10.20944/preprints202105.0562.v1

for RWGS reactions.

1. Introduction

Carbon-neutral technologies have attracted increasing attention over the last two decades because of global warming and climate change caused by excessive CO_2 emissions [1-3]. Several strategies have great potential to convert captured CO_2 to synthetic fuels i.e. (1) the RWGS reaction [4,5], (2) CO_2 direct hydrogenation [6-8], (3) methane dry reforming [9,10], and (4) CO_2 to Lower Olefins [11-13]. CO_2 reduction to CO through the RWGS reaction is an attractive process, because not only does it produce CO, a very useful chemical, it also plays a vital role in many CO_2 hydrogenation reactions [4-13]. The RWGS is thermodynamically favorable at high temperature because of its endothermic nature ($CO_2 + H_2 \leftrightarrow CO + H_2O$, $\Delta H = 41.3$ kJ/mol). Therefore, the activity and thermal stability of catalysts are two main concerns in developing RWGS catalysts [3].

Noble metal catalysts present good low temperature activity and stability in RWGS [14-16], but the high price and low reserve hindered their applications. Transition metal catalysts, typically the copper catalysts [17-19], which are more acceptable in price, have been extensively researched. But the stability of transition metal catalysts at high temperature is still great challenges [3,20]. It is interesting that mixed main group metal oxides also show good activity and stability, such as $BaZr_{0.8}Y_{0.2}O_3$ and $BaZr_{0.8}Y_{0.16}Zn_{0.04}O_3$ [21]. Oxygen vacancies might play an important role in the activity of metal oxides in RWGS reactions. However, insertion of additional Ce into the structure of metal oxides (introducing more defects) did not have any positive effect on the catalytic activity for the RWGS reaction and even lowered down the thermal stability of catalysts. Recently, spinel catalysts (Cu-Al and Co-Al) containing transition metal oxides as promising candidates for CO_2 conversion to CO were reported [22,23]. Unlike other copper-based catalysts, spinel catalysts have both high activity and high stability in RWGS reaction. And under-coordinated transition metal-oxygen ligands were considered as the active sites for CO_2 adsorption and activation on the spinel surfaces [22.23]. However, the related reaction mechanism are still unclear.

Reaction mechanisms of RWGS can be classified into two categories, i.e., redox mechanism [24,25] and hydrogenation mechanism (through formate (HCOO) or carboxyl (COOH)) [26,27]. The major difference lies in whether hydrogen species involves in the formation of carbon-containing intermediates. RWGS reaction via redox mechanism often consists of a successive rapid alternation on the active sites with oxidation↔reduction loops. Therefore, noble metal loading on reducible oxide supports with good redox properties may have excellent RWGS activity, such as Au-CeO_2 [28-30]. For the hydrogenation mechanism, the formation of formate or carboxyl is considered as the critical step of the RWGS process. Hence, transition metal loading on Brønsted acidic supports may be active in RWGS reaction, such as Cu-ZnO [31], Cu-MgO [32] and Pt-TiO_2 [33]. It should be noticed that both of the two routes may be feasible on a given metal/oxide catalysts [34].

In this work, $MgAl_2O_4$ spinel catalyst without transition metal oxides was found to be active in RWGS at high temperatures. And the H_2O formation ($OH^* + H^* \rightarrow H_2O^* + {}^*$) on spinel was considered as the rate determining step in RWGS over $MgAlO_4$ rather than the hydrogenation or the direct dissociation of CO_2.

2. Experimental section

2.1 Materials Preparation

Materials. $Mg(NO_3)_2{\cdot}6H_2O$ (99+%, Acros Organics) and C_3H_6O (99.5%, Acros Organics) were purchased from Aladdin Industrial Corporation. $Ni(NO_3)_2{\cdot}6H_2O$ (99+%, Acros Organics) and $Al(NO_3)_3{\cdot}9H_2O$ (99+%, Acros Organics) were purchased from Sinopharm Chemical Reagent Co.LTD. C_2H_5OH (99.7%, Acros Organics) was purchased from Xilong Scientific. Deionized water was obtained from a laboratory purification system.

Synthesis. Preparation of $MgAl_2O_4$. $MgAl_2O_4$ was prepared by sol-gel method [35]. A certain amount of $Mg(NO_3)_2{\cdot}6H_2O$ and $Al(NO_3)_3{\cdot}9H_2O$ was solved in anhydrous ethanol: each 0.01 mol $MgAl_2O_4$ corresponds to 70 ml of anhydrous ethanol. After that, C_3H_6O was drop wise added into the nitrate solution under stirring at 70°C to obtain the gel. The obtained gel was dried at 80 °C for 24 h and then treated at 800 °C for 2 h in muffle furnace with a temperature elevating rate of 3 °C /min.

Preparation of 0.5 wt.% $Ni/MgAl_2O_4$ Catalyst (denoted Nano $Ni/MgAl_2O_4$). The Nano $Ni/MgAl_2O_4$ catalyst preparation process is consistent with the above mentioned $MgAl_2O_4$ while adding the required amount of $Ni(NO_3)_2{\cdot}6H_2O$ replacing corresponding amount of the $Mg(NO_3)_2{\cdot}6H_2O$.

doi:10.20944/preprints202105.0562.v1

Preparation of Ni Single Atom/$MgAl_2O_4$ Catalyst (denoted Ni (SA)/$MgAl_2O_4$). Ni (SA)/ $MgAl_2O_4$ was prepared by acid leaching [36]. 0.5 g Nano Ni samples were put into 30 mL sulfuric acid solution with pH=2, stirred and leached at room temperature for 2.5 h. Then, the leached samples were centrifuged in deionized water until the solution reaching pH neutral. Then the products were dried at 80 °C for 24 h.

2.2 Characterization

ICP. The actual Ni content was determined by inductively coupled plasma-optical emission spectrometry (ICP- OES, Thermo IRIS Intrepid II).

XRD. The X-ray diffraction (XRD) measurement was used to characterize the crystalline structure of the catalysts. The spectra were collected on the D8 Advance X-ray diffractometer (XRD) using Cu Kα radiation with a scanning angle (2θ) of 15~90°. Analysis of XRD test data and calculation of lattice parameters were performed on JADE software (JADE version 5, Materials Data, Inc.).

*BET. BET s*urface area and BJH pore volume of catalyst were measured on ASAP 2020 M + C by applying N_2 adsorption isotherms and BET analysis methods. Before testing, all of the samples were degassed at 150 °C in a vacuum for 4 h.

TEM and STEM. The $MgAl_2O_4$ and Nano Ni/ $MgAl_2O_4$ sample's structures were characterized using a transmission electron microscope FEI TECNAI G2 F30 with scanning TEM (STEM) and high resolution TEM (HRTEM) modes. The single atomic Ni^{n+} species were characterized by spherical aberration corrected Transmission Electron Microscope (ACTEM) Titan ETEM Themis.

EXAFS. Extended X-ray absorption fine structure spectra (EXAFS) at Ni K-edge were collected at the Singapore Synchrotron Linght Source (SSLS) center, in which the X-ray beam was monochromatized with channel-cut Si (111) crystals. The Ni K-edge absorption data was recorded in a transmission mode. Ni foil and NiO were used as references. The storage ring was working at the energy of 2.5 GeV with an average electron current of below 200 mA. The acquired EAXFS data were extracted and processed according to the standard procedures using the ATHENA module implemented in the IFEFFIT software packages. The k3-weighted Fourier transform (FT) of χ (k) in R space was obtained over the range 0-14.0 Å^{-1} by applying a Bessel window function.

XPS. The chemical states of these catalysts were characterized by X-ray photoelectron spectra (XPS, PHI-5000 Versaprobe II) equipped monochromatic Al Kα (1486.6 eV), operated at 15 KV and 50 W. The binding energy (BE) was calibrated using the 1*s* peak of C at 284.8 eV. The spectra lines were smoothed via the Fourier smoothing method and fitted using a symmetric pseudo-Voigt function called GL (30) in CasaXPS software.

H_2-TPR. Temperature-programmed reduction (H_2-TPR) was performed on a Micromeritics Autochem 2920 II instrument. Typically, the sample (cat. 50 mg) was loaded into a U-shaped quartz reactor and dried for 1 h under Ar flow (40 mL min^{-1}) at 120 °C (5 °C min^{-1}). After cooling down to room temperature, switched the flow to a 10 vol% H_2/Ar，and ramped to 860 °C at 10 °C min^{-1} with flow rate 40mL min^{-1}. During this process, H_2 consumption was monitored using a calibrated thermal conductivity

detector (TCD).

In situ DRIFTS. The in situ DRIFTS were collected in the range of 400~4000 cm^{-1} using a Bruker Vertex 70V FTIR spectrometer equipped with a liquid nitrogen refrigeration MCT detector. Before measurement, Nano Ni/$MgAl_2O_4$ and Ni (SA)/$MgAl_2O_4$ were pre-reduced at 800 °C in 5vol % H_2 for 2 h. For each measurement, 15 mg of catalyst was placed in the cell, heated up to the test temperature in 5vol %H_2 flow and then stabilized in Ar for 30 min to ensure the complete removal of adsorbed species. Then switching to 5vol % CO_2， the first point was collected after 30 min. Next, shutting off CO_2, 5vol %H_2 was introduced and the second point was recorded after 10 min.

Catalytic Tests. All catalytic tests were performed in a fixed bed reactor under ambient pressure. 20 mg sample (60 mesh) was loaded into a 10 mm inner diameter quartz reactor tube. The bed was heated to 800 °C at a ramp rate of 10 °C min^{-1} under 5 vol.% H_2/Ar (100 mL min^{-1}) and held for 2.5 h to activate the catalyst in situ. Then, the gas mixture (5 vol.% CO_2, 5 vol.% H_2, He as the equilibrium) was introduced to the reactor with a total flow of 75 mL min^{-1} (weight hourly space velocity (WHSV) = 225000 mL/(g·h). Gas analysis was performed online by a gas chromatograph (FULI GC9790Plus) equipped with a thermal conductivity detector to analyze H_2、CO and CO_2.

2.3 Density functional theory (DFT) Calculation Details

The first-principle calculations were performed with the Vienna Ab-inito Simulation Package (VASP). The ion-electron interactions were treated with the projectedaugmented wave (PAW) method. The exchange-correlation interactions were calculated with the PBE scheme. The energy cut-off was set to 400 eV, and the self-consistent convergence was set at criteria of 0.0001 eV/atom. The spin polarization was considered in the calculation. For the $MgAl_2O_4$-(111) surface structure, a 1×1 two-dimensional supercell consisting of four layers was constructed, which contains 16 Mg, 32 Al and 64 O atoms, and the vacuum layer was set at more than 20.0 Å. For the single Ni atom doped $MgAl_2O_4$-(111) surface, only a Al atom on the surface was replaced by Ni atom.

For each step, the free energy differences are calculated with:

$$\Delta G = \Delta E + \Delta ZPE + T\Delta S$$

Where ΔE is the total energy difference between the neighboring states calculated from DFT calculation, ΔZPE is the difference of the zero point energy, ΔS is the difference of entropies, and the temperature is set at 700 K.

3. Results and discussion

3.1.Structure of Catalysts

The content of Ni in Nano Ni/$MgAl_2O_4$ and Ni (SA)/$MgAl_2O_4$ by ICP-OES is 0.43 wt.% and 0.21 wt.% respectively. BET and BJH results are shown in **Table 1**.

Table1. BET and BJH results of three catalysts

Catalysts	S_{BET} (m^2 g^{-1})	V_m (cm^3 g^{-1})	V_P (cm^3 g^{-1})	Mean pore diameter (nm)
Nano Ni/$MgAl_2O_4$	121.69	27.958	0.3159	10.477

Ni (SA)/$MgAl_2O_4$	131.62	30.241	0.2641	8.2591
$MgAl_2O_4$	125.35	28.8	0.3406	10.953

The XRD patterns of catalysts are shown in **Fig. 1**a. All catalysts present well-crystallized spinel phase. Three sharp peaks at 2θ = 36.951°, 44.956° and 65.441° are ascribed to the (3 1 1), (4 0 0), (4 4 0) planes of cubic $MgAl_2O_4$ (JCPDS Card No. 21-1152). No characteristic peaks of nickel species can be detected indicating that Ni species uniformly distribute on $MgAl_2O_4$ or are in the matrix of $MgAl_2O_4$. From **Fig. 1**b and c, the lattice parameters of $MgAl_2O_4$ (8.0559 pm) expands to (8.0695 pm) when nickel doped into the lattice matrix of spinel because of the bigger ionic radius of Ni^{2+} (0.55 Å) than those of Al^{3+} ions (0.535 Å) [37]. The HRTEM image in **Fig. 1**d shows that $MgAl_2O_4$ are lamella particles in diameter of ~13 nm. Ni nanoparticles on nano Ni/$MgAl_2O_4$ are in size of 2~5 nm (**Fig. 1**e). After acid leaching, no nano nickel species but single atomic Ni can be found on Ni (SA)/$MgAl_2O_4$ (**Fig. 1**f).

The local coordination structure of Ni atoms in Ni (SA)/$MgAl_2O_4$ was revealed by the phase corrected Fourier transformation of EXAFS spectroscopy (FT-EXAFS). The X-ray absorption near edge (XANE) curves **(Fig. 1**g) indicate that the Ni atoms in Ni (SA)/$MgAl_2O_4$ are cations but different with Ni^{2+} of NiO. The Ni K edge of Ni (SA)/$MgAl_2O_4$ shows just one main peak at ~1.65 Å in the R-space spectrum (**Fig. 1**h) without peaks of Ni-Ni at ~2.18 Å and with only weak peak of Ni^{2+}-O^{2-}-Ni^{2+} at ~2.60 Å (**Fig. 1**i) [38], suggesting that Ni^{n+} ions in Ni (SA)/$MgAl_2O_4$ are highly dispersed in the lattice matrix of spinel and the Ni^{n+}-O^{2-} species are isolated by Al^{3+} ions. This result can also be verified by wavelet transform (WT) based on its ultra-high resolution in k and R spaces. The Ni K-edge WTEXAFS of Ni (SA)/$MgAl_2O_4$ is shown in **Fig. 1**j~**1**l, with references of Ni foil and NiO in **Fig. 1**k and **Fig. 1**l respectively. The signals related to Ni-Ni coordination and Ni^{2+}-O^{2-}-Ni^{2+} were not probed. The distribution of Ni elements on Ni (SA)/$MgAl_2O_4$ is dominated by single atoms. The detailed modeling parameters of Ni (SA)/$MgAl_2O_4$ are shown in **Table 2**. The coordination of Ni with O is 5.6 ± 0.6 indicating that the single atomic Ni ions (Ni^{n+}, $2<n<3$) occupy the Al^{3+} sites, which is consistent with the DFT calculation results (discussed later).

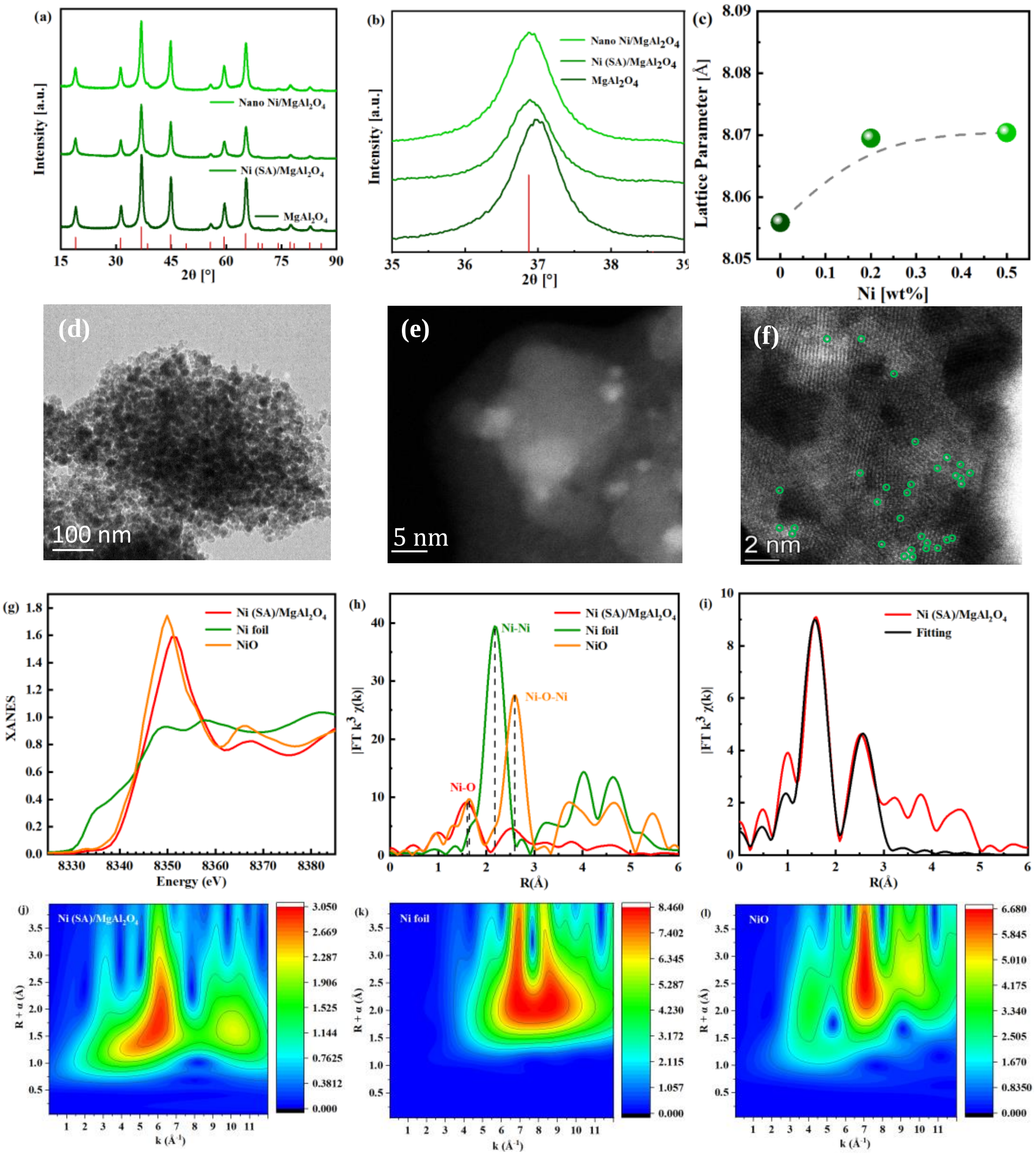

Figure 1. (a) XRD patterns of catalysts; (b) Angle shift of the (3 1 1) plane, zoom in the 35~39° region; (c) lattice parameters of catalysts; (d) HRTEM image of $MgAl_2O_4$; (e) HAADF-STEM

image of Nano Ni/$MgAl_2O_4$; (f) AC-HAADF-STEM image of Ni (SA)/$MgAl_2O_4$; (g) XANES and (h) FT-EXAFS spectra of Ni (SA)/$MgAl_2O_4$ with references of Ni foil and NiO; (i) Experimental (red) and fitting curves (black) of Ni K edge of Ni (SA)/$MgAl_2O_4$; (j) WT-EXAFS of Ni (SA)/$MgAl_2O_4$; (k) WT-EXAFS of Ni foil; (l) WT-EXAFS of NiO.

Table 2. EXAFS modeling parameters of Ni (SA)/$MgAl_2O_4$

samples	shell	CN	R(Å)	σ^2	ΔE_0	R factor
Ni (SA)/$MgAl_2O_4$	Ni-O	5.6 ± 0.6	2.02 ± 0.02	0.0034	-7.0 ± 2.6	0.0188
	Ni-Ni	1.7 ± 1.0	2.59 ± 0.05	0.0128		
	Ni-O-Ni	5.6 ± 1.7	3.06 ± 0.03			

[a]*N*: coordination numbers; [b]*R*: bond distance; [c]σ^2: Debye-Waller factors; [d] ΔE_0: the inner potential correction. *R* factor: goodness of fit. S_0^2 was set to 0.76, according to the experimental EXAFS fit of Ni foil reference by fixing CN as the known crystallographic value; δ: percentage.

XPS spectra were measured to determine the local chemical environment of each element and the results are shown in **Fig. 2**. The obtained spectra of Ni $2p_{3/2}$ (870~850 eV) have strong satellite peaks at 861.6 eV in Nano Ni/$MgAl_2O_4$ (**Fig. 2**b), attributing to the long-range scattering of structural -Ni-O-Ni-O-·in the lattice of NiO crystals. However, no satellite peak can be observed in Ni (SA)/$MgAl_2O_4$ (**Fig. 2**b), consolidating the single atomic state of Ni^{n+}. Besides, the $2p_{3/2}$ binding energy of Ni^{n+} ions in Ni (SA)/$MgAl_2O_4$ is at 857.0 eV which is significantly higher than that of Nano

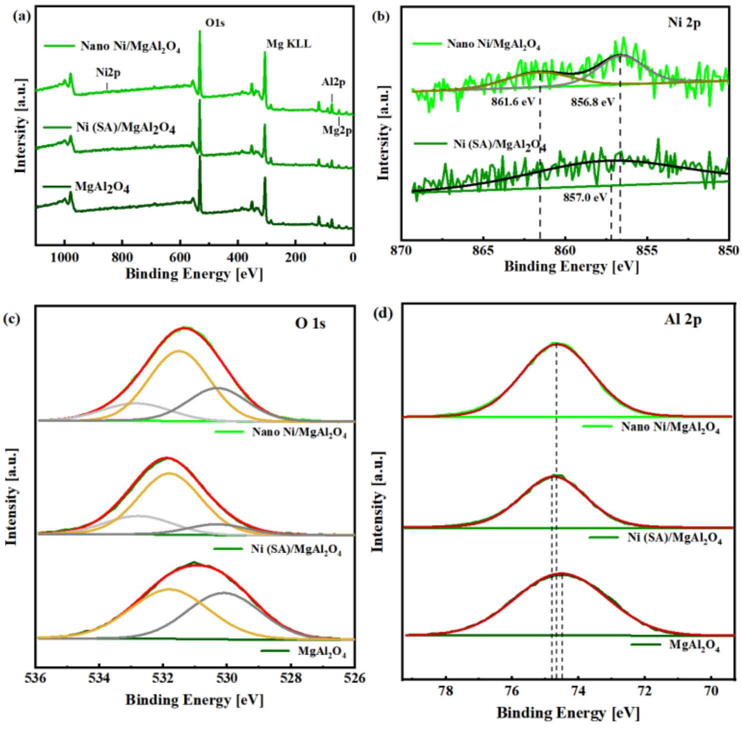

Ni/$MgAl_2O_4$ at 856.8 eV, also verifying a more positive oxidative state of Ni^{n+} than Ni^{2+} [39]. More positive of Ni^{n+} arising from the interaction between nickel and $MgAl_2O_4$ may result in more oxygen vacancies and then lead to more negative hydroxyl groups on the surface of Ni (SA)/$MgAl_2O_4$ catalyst arising from the reaction between H_2O and oxygen vacancies ($H_2O^* + V_O^* \rightarrow OH^* + H^*$).

Figure 2. (a) full XPS spectrum of catalysts; (b) Ni 2*p* spectra; (c) O 1*s* spectra; (d) Al 2*p* spectra

The O 1*s* spectrum of $MgAl_2O_4$ is deconvoluted into two main peaks (**Fig. 2**c). The peak at 530.1 eV refers to the lattice oxygen (O_L), another peak at 531.8 eV is attributing to the surface oxygen vacancy defect or low-coordinated oxygen ions (O_D). However, a new fitting peak appears at 533.0 eV after introducing nickel into $MgAl_2O_4$, which can be attributed to hydroxyl-type oxygen species (OH^-), designated as O_H [40,41]. The detailed results of O 1*s* spectra are shown in **Table 3**.

Table 3. XPS results for the three catalysts : binding energies (eV) ; full width at half maximum (FWHM) ; relative percentages (%Area).

Catalysts	O_L (530.1 eV)		O_D (531.8 eV)		O_H (533.0 eV)	
	%Area	FWHM	%Area	FWHM	%Area	FWHM
Nano Ni/$MgAl_2O_4$	27.64	2.17	56.47	2.22	15.88	2.51
Ni (SA)/$MgAl_2O_4$	11.41	2.20	67.64	2.32	20.96	2.50
$MgAl_2O_4$	45.39	2.69	54.61	2.89	0	--

The O_H contention in Ni (SA)/$MgAl_2O_4$ (20.96%) is much higher than those on Nano Ni/$MgAl_2O_4$ (15.88%) and far higher than that of pristine $MgAl_2O_4$ (0%), indicating that O_H may arise from the defect introduced by Ni^{n+} on the interface nickel and $MgAl_2O_4$. The presence of O_H on catalyst may have an important effect on the RWGS reaction. This conclusion will be confirmed later on by in situ FITR. In addition, the binding energy of Al^{3+} ions in Ni (SA)/$MgAl_2O_4$ and Nano Ni/$MgAl_2O_4$ is at 74.8 eV and 74.7 eV respectively, which are both higher than that of $MgAl_2O_4$ at 74.5 eV. Because the Al^{3+} sites were occupied by Ni^{n+}, leading to more positive Al^{3+} to obtain the surface charge balance.

3.2. Catalytic performance of catalysts in RWGS

Catalytic performances of three catalysts ($MgAl_2O_4$, Nano Ni/$MgAl_2O_4$ and Ni (SA)/$MgAl_2O_4$ in RWGS were studied on a fixed-bed flow reactor in the temperature range of 600~800 °C **(Fig. 3**a). Surprisingly, as an extremely stable support, $MgAl_2O_4$ showed remarkable activity in RWGS at temperatures higher than 600°C, the CO_2 conversion rate reached 37.76% at 800 °C. To be rigorous, we also tested the CO_2 conversion in RWGS reaction without catalyst at 800 °C, and the conversion rate of CO_2 was zero. Loading Ni nanoparticles on $MgAl_2O_4$ improves the CO_2 conversion remarkably. Interestingly, leaching out the Ni nanoparticle on $MgAl_2O_4$ will obtain much more active catalyst in RWGS, the CO_2 conversion rate reached 46.3% at 800 °C, almost reaching the thermodynamic equilibrium conversion [42]. The conversion of CO_2 even remained stable after 75 h of durability test at 800 °C and high weight hourly space velocities (225 000 ml g^{-1} h^{-1}), as shown in **Fig. 3**b. In addition, no by-products were detected during the reaction of the three catalysts.

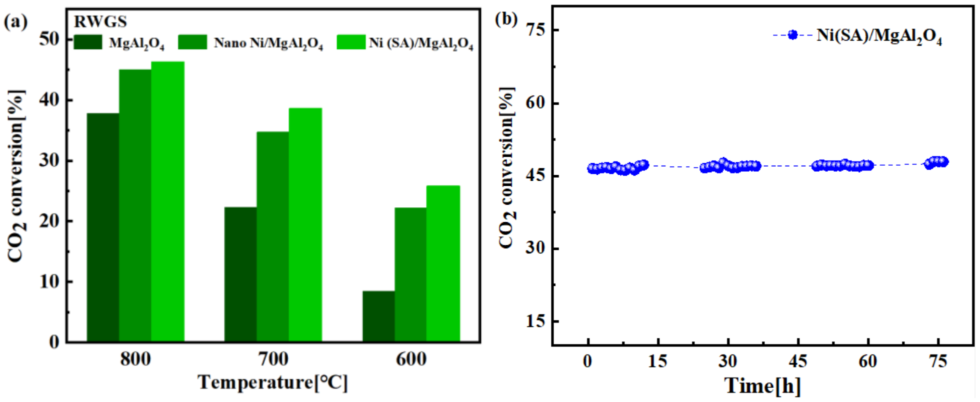

Figure 3. (a) Catalytic performances of three samples ($MgAl_2O_4$, Nano Ni/$MgAl_2O_4$ and Ni (SA)/$MgAl_2O_4$) for RWGS in the temperature range of 600~800 °C. (b) Endurance test of Ni (SA)/$MgAl_2O_4$ for RWGS at 800 °C.

3.3. In situ FITR of RWGS reactions on catalyst

In situ FITR was performed to investigate the surface species over catalysts under operando conditions and the results are shown in **Fig. 4**. Generally, the CO_2 and H_2 derived species on $MgAl_2O_4$ and Ni (SA)/$MgAl_2O_4$ are quiet similar, indicating the reactions proceed the similar routes. After introducing 5% CO_2, the spectral features formed at 1642 cm^{-1} clearly demonstrate the formation of surface bicarbonates, which are generated from the reaction between CO_2 and hydroxyl groups on $MgAl_2O_4$ [43]. The bicarbonate peak increased obviously on Nano Ni/$MgAl_2O_4$ and Ni (SA)/$MgAl_2O_4$ due to more surface hydroxyl groups on nickel doped $MgAl_2O_4$. The weak bands at 1380 cm^{-1} and 2910 cm^{-1} indicate that CO_2 can react with the protons of hydroxyl groups to generate formate [44-46]. The adsorption band of CO^* was not observed in the FITR spectrum because of the weak adsorption energy of CO^* species on $MgAl_2O_4$ [47]. After switching to H_2 flow, the signals of bicarbonates decreased quickly while the formate peaks increase. This result suggests that formate is easy to generate but difficult to decompose, which means the “formate route” is not the optimal path. The

DFT calculation below also proves this conclusion. X. Wang [46] and L.F. Bobadilla [40] demonstrated the formate mechanism of RWGS on Pd/Al_2O_3 and Au/Al_2O_3. The peaks at 2295 cm^{-1} and 2374 cm^{-1} were attributed to the physical adsorbed CO_2 [44]. In this work, these two peaks are weakened significantly on Ni (SA)/$MgAl_2O_4$, indicating that CO_2 is prone to adsorb on Al^{3+} sites. Acid leaching leads to the decrease of surface of surface Al^{3+} ions.

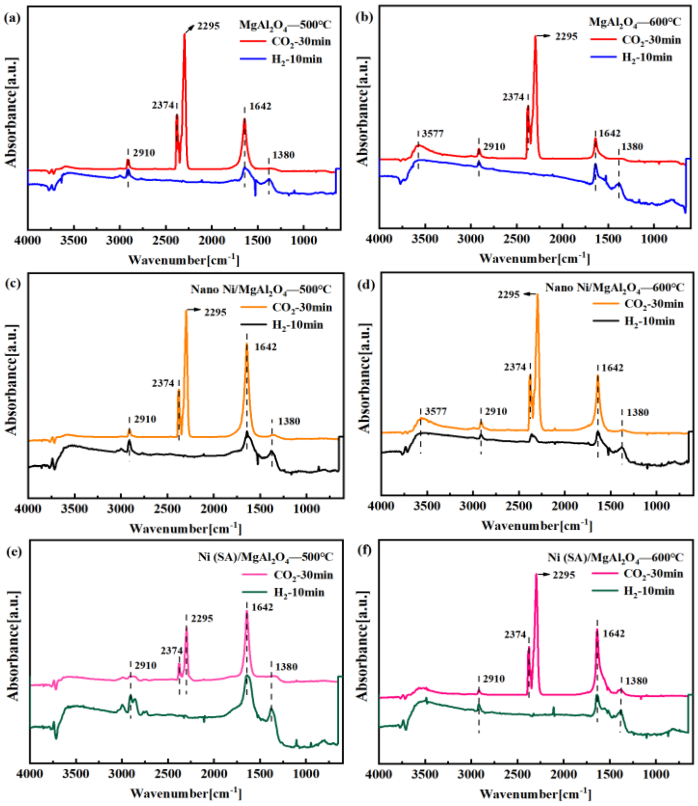

Figure 4. In-situ DRIFT spectra of catalysts at 500 °C: (a) $MgAl_2O_4$, (c) Nano Ni/$MgAl_2O_4$, (e) Ni(SA)/$MgAl_2O_4$. In-situ DRIFT spectra at 600 °C: (b) $MgAl_2O_4$, (d) Nano Ni/$MgAl_2O_4$, (f) Ni (SA)/$MgAl_2O_4$.

3.4. Density functional theory (DFT) calculations

Density functional theory (DFT) method was performed to investigate the adsorption sites, geometries of intermediate species and possible reaction paths of RWGS reactions

doi:10.20944/preprints202105.0562.v1

on (111) surface of $MgAl_2O_4$ and Ni (SA)/$MgAl_2O_4$.

The primitive cell structure and the geometries of adsorbed species on $MgAl_2O_4$ and Ni (SA)/$MgAl_2O_4$ are shown in **Fig. S1** and **S2**. Based on the model, the active adsorption site was Al^{3+} on $MgAl_2O_4$ (111) surface (**Fig. S1**): one CO_2 molecule adsorbs on two adjacent Al^{3+} sites in bridge style. However, when single atomic Ni doped into the (111) surface of $MgAl_2O_4$, the adsorption site of CO_2 alters to one Al^{3+} site near the Ni^{n+} ion. CO_2 can be directly dissociated into CO^* (redox mechanism), or combined with H^* to form $COOH^*$ or $HCOO^*$. Then $COOH^*$ formed CO by removing OH^*, while dissociation of $HCOO^*$ would produce HCO^* and O^*, followed by dehydrogenation of HCO^* to form CO. The detailed energy barriers of elementary steps for RWGS are shown in **Table 4**, and the potential diagrams calculated by DFT on $MgAl_2O_4$ and Ni (SA)/$MgAl_2O_4$ are shown in **Fig. 5**.

Three reaction routes were proposed, the “redox mechanism”, the “formate route” and the “carboxyl route”. From the energy view, the “carboxyl route” may be more possible for the RWGS process on both catalysts rather than the “formate route” and “redox mechanism”. The rate limiting step is strongly depend on the surface structure. The free energy differences of the above reactions on $MgAl_2O_4$ and Ni(SA)/$MgAl_2O_4$ clearly demonstrates that there are strong interactions between the surface and the absorbed molecules, such as CO^*, O^*, OH^* and HCO^*, which is mainly due to the dangling bond of the surface. This make the CO_2 decomposition is easily. Also due to the large absorbed energies of O^* and OH^* on the surface, the ΔG of the reaction “$OH^* + H^* \rightarrow$

$H_2O^* + {}^*$” largely increases, which means it is the rate limiting step (RDS). The energy barrier of RDS is significantly reduced from 2.85 eV to 1.68 eV after introducing Ni^{n+} into $MgAl_2O_4$. Due to the under coordination state of Ni^{2+} in $MgAl_2O_4$, the ligand oxygen needs to retrieve more electrons from nearby Al^{3+}, leading to more positive Al^{3+} (XPS results) and hence the reduced bonding energy between Al^{3+} and adsorbates. So, the ΔG of reaction ($CO_2^* + {}^* \rightarrow CO^* + O^*$), reaction ($O^* + H^* \rightarrow OH^* + {}^*$) and reaction ($OH^* + H^* \rightarrow H_2O^* + {}^*$) on Ni (SA)/$MgAl_2O_4$ are remarkably reduced compared with those of $MgAl_2O_4$.

Scheme 1 shows the possible RWGS reaction network, including three CO_2 activation steps and pathways which are similar to those reported on transition metal phosphides and Au/Al_2O_3 [38,45].

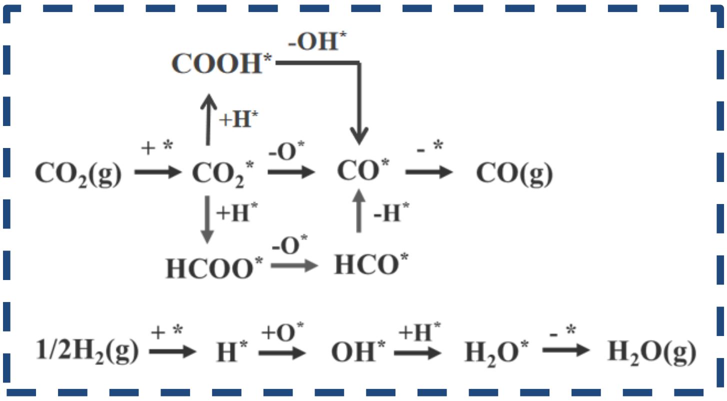

Scheme 1. Three pathways of CO_2 activation and the reaction scheme from H_2 to H_2O

Table 4. Reaction energy (Δ*G*) and activation barrier (*E*a) of the RWGS elementary steps on $MgAl_2O_4$ and Nano Ni/$MgAl_2O_4$.

No.	Elementary steps	$MgAl_2O_4$		Ni (SA)/$MgAl_2O_4$	
		Δ*G*/eV	E_a/eV	Δ*G*/eV	E_a/eV
1	$CO_2(g) + {}^* \rightarrow CO_2^*$	-0.49	——	-0.92	——
2	$CO_2^* + {}^* \rightarrow CO^* + O^*$	-2.81	0.65	-0.51	0.82
3	$CO_2^* + H^* \rightarrow COOH^* + {}^*$	0.72	0.83	0.38	0.90
4	$COOH^* \rightarrow CO^* + OH^*$	-2.42	0.42	-0.82	0.15

5	$CO_2^* + H^* \rightarrow HCOO^* + {}^*$	-0.36	0.1	-0.01	0.49
6	$HCOO^* \rightarrow HCO^* + O^*$	-0.27	0.42	-1.58	0.83
7	$HCO^* \rightarrow CO^* + H^*$	-0.37	0.12	1.08	1.44
8	$1/2\ H_2(g) + {}^* \rightarrow H^*$	-0.48	——	0.06	——
9	$O^* + H^* \rightarrow OH^* + {}^*$	1.10	1.63	0.07	1.48
10	$OH^* + H^* \rightarrow H_2O^* + {}^*$	2.73	2.85	1.56	1.68
11	$H_2O^* \rightarrow {}^* + H_2O(g)$	0.05	——	-0.21	——
12	$CO^* \rightarrow {}^* + CO(g)$	0.91	——	0.42	——

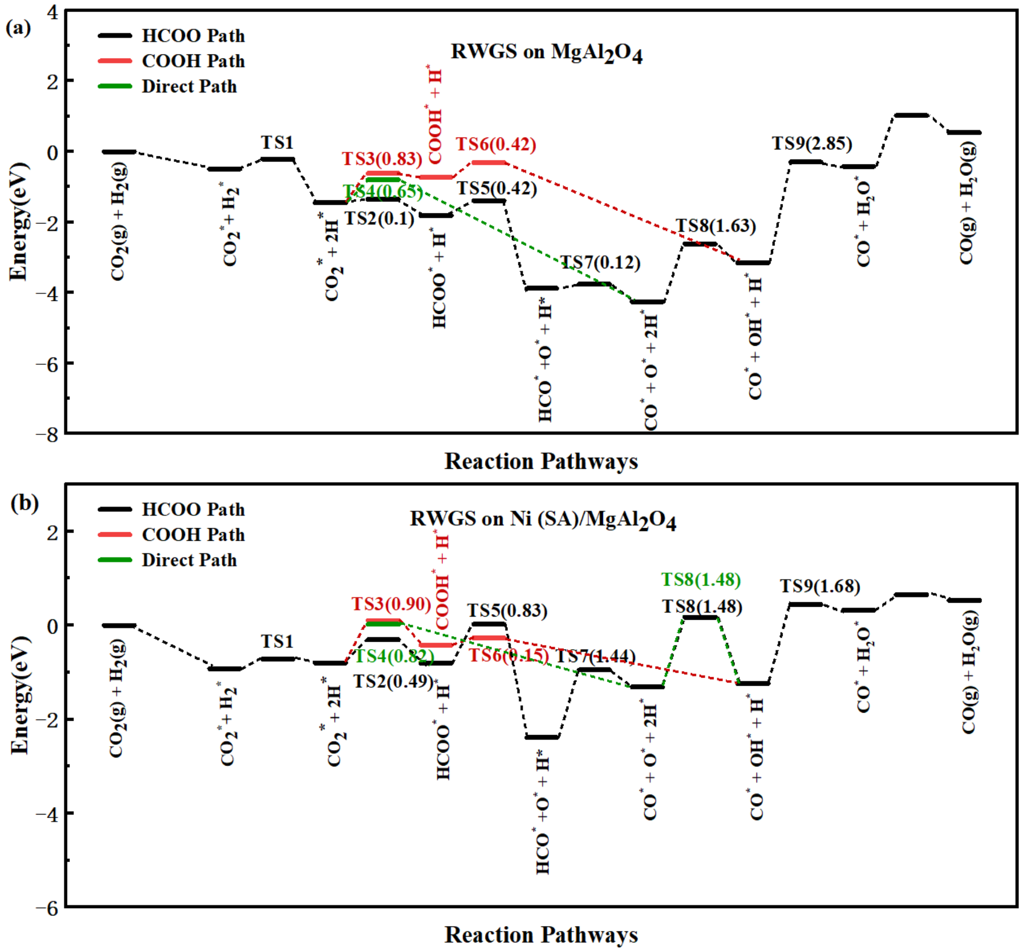

Figure 5. Potential energy for RWGS reaction on (a) $MgAl_2O_4$ (111) and (b) Ni (SA)/$MgAl_2O_4$ (111) surfaces.

4. Conclusion

In this work, $MgAl_2O_4$ was found to be an active catalyst in RWGS reaction at temperatures higher than 600°C. Mechanism study revealed that $OH^* + H^* \rightarrow H_2O^* + {}^*$ is the rate determination step in RWGS on $MgAl_2O_4$ and Ni (SA)/$MgAl_2O_4$. The energy barrier is significantly reduced after adding single atomic Ni^{n+} into the matrix of spinel. The "-COOH path" may proceed most easily over $MgAl_2O_4$ or Ni^{n+} doped $MgAl_2O_4$ at high temperatures.

Corresponding Author:

*Email: si.zhichun@sz.tsinghua.edu.cn

Associated Content

Supporting Information

The adsorption structures of intermediate species on $MgAl_2O_4$ and Ni (SA)/$MgAl_2O_4$ (111) surfaces.

Author Contributions:

Zhichun Si initiates the research. Lingling Zhang prepared and characterized the catalysts. Lingling Zhang and Zhichun Si did the DFT calculation and wrote the manuscript. Qi Song, Rui Ran, Xiaodong Wu, Duan Weng and Feiyu Kang helped characterize the catalysts.

Acknowledgements

The authors would like to acknowledge the Strategic Emerging Industry Development Funds of Shenzhen (JCYJ20170817161720484).

Declaration of Competing Interest

The authors declare no conflict of interest in this paper.

References

[1] Dennis U., Nielsen, Xin-Ming, Hu, Kim, Daasbjerg, Troels, Skrydstrup, Chemically and electrochemically catalysed conversion of CO_2 to CO with follow-up utilization to value-added chemicals, Nature Catalysis. 1 (2018) 244-254.

[2] S.B. Jo, J.H. Woo, J.H. Lee, T.Y. Kim, H.I. Kang, S.C. Lee, J.C. Kim, CO_2 green technologies

in CO_2 capture and direct utilization processes: methanation, reverse water-gas shift, and dry reforming of methane, Sustainable Energy & Fuels. 4 (2020) 5543-5549.

[3] M. S. Duyar, M. A. A. Treviño, Farrauto, R. J., Dual function materials for CO_2 capture and conversion using renewable H_2, Applied Catalysis B Environmental. 168 (2015) 370-376.

[4] X. Chen, Y. Chen, C. Song, P. Ji, L. Cui, Recent Advances in Supported Metal Catalysts and Oxide Catalysts for the Reverse Water-Gas Shift Reaction, Frontiers in Chemistry, 8 (2020) 709.

[5] X. Su, X. Yang, B. Zhao, Y. Huang, Designing of highly selective and high-temperature endurable RWGS heterogeneous catalysts: recent advances and the future directions, Journal of Energy Chemistry, 26 (2017) 854-867.

[6] F. Studt, I. Sharafutdinov, F. Abild-Pedersen, C.F. Elkjær, J.S. Hummelshøj, S.R. Dahl, I. Chorkendorff, J.K. Nørskov, Discovery of a Ni-Ga catalyst for carbon dioxide reduction to methanol, Nature Chemistry, 6 (2014) 320-324.

[7] X. Jiang, X. Nie, X. Guo, C. Song, J.G. Chen, Recent Advances in Carbon Dioxide Hydrogenation to Methanol via Heterogeneous Catalysis, Chemical Reviews, 120 (2020) 7984-8034.

[8] S. Kattel, P.J. Ramírez, J.G. Chen, J.A. Rodriguez, P. Liu, Active sites for CO_2 hydrogenation to methanol on Cu/ZnO catalysts, Science, 357 (2017) 1296-1299.

[9] D. Pakhare, J. Spivey, A review of dry (CO_2) reforming of methane over noble metal catalysts, Chemical Society Reviews, 43 (2014) 7813-7837.

[10] J. Won-Jun, S. Jae-Oh, K. Hak-Min, Y. Seong-Yeun, R. Hyun-Seog, A review on dry reforming of methane in aspect of catalytic properties, Catalysis Today, 324 (2018) 15-26.

[11] X. Liu, M. Wang, H. Yin, J. Hu, Y. Wang, Tandem Catalysis for Hydrogenation of CO and CO_2 to Lower Olefins with Bifunctional Catalysts Composed of Spinel Oxide and SAPO-34, ACS Catalysis, 10 (2020) 8303-8314.

[12] L. Guo, J. Sun, X. Ji, J. Wei, Z. Wen, R. Yao, H. Xu, Q. Ge, Directly converting carbon dioxide to linear α-olefins on bio-promoted catalysts, Communications Chemistry, 1 (2018) 11-18.

[13] M.K. Khan, P. Butolia, H. Jo, M. Irshad, J. Kim, Selective Conversion of Carbon Dioxide into Liquid Hydrocarbons and Long-Chain α-Olefins over Fe-Amorphous AlOx Bifunctional Catalyst, ACS Catalysis, 10 (2020) 10325-10338.

[14] N.C. Nelson, L. Chen, D. Meira, L. Kovarik, J. Szanyi, InSitu Dispersion of Palladium on TiO_2 During Reverse Water-Gas Shift Reaction: Formation of Atomically Dispersed Palladium, Angewandte Chemie, 59 (2020) 17657-17663.

[15] Y. Tang, C. Asokan, M. Xu, G.W. Graham, P. Sautet, Rh single atoms on TiO_2 dynamically respond to reaction conditions by adapting their site, Nature Communications, 10 (2019) 1-10.

[16] S. Kattel, B. Yan, J.G. Chen, P. Liu, CO_2 hydrogenation on Pt, Pt/SiO_2 and Pt/TiO_2: Importance of synergy between Pt and oxide support, Journal of Catalysis, 343 (2016) 115-126.

[17] J. Schumann, M. Eichelbaum, T. Lunkenbein, N. Thomas, M.C. álvarez Galván, R. Schlögl, M. Behrens, Promoting Strong Metal Support Interaction: Doping ZnO for Enhanced Activity of Cu/ZnO:M (M = Al, Ga, Mg) Catalysts, ACS Catalysis, 5 (2015) 3260-3270.

[18] X. Zhang, X. Zhu, L. Lin, S. Yao, M. Zhang, X. Liu, X. Wang, Y.W. Li, C. Shi, D. Ma, Highly Dispersed Copper over β-Mo_2C as an Efficient and Stable Catalyst for the Reverse Water Gas Shift (RWGS) Reaction, ACS Catalysis, 7 (2017) 912-918.

[19] C.l. Galván, J. Schumann, M. Behrens, J.L.G. Fierro, E. Frei, Reverse Water-Gas Shift

Reaction at the Cu/ZnO interface: Influence of the Cu/Zn ratio on structure-activity correlations, Applied Catalysis B Environmental, 195 (2016) 104-111.

[20] S. Choi, B.I. Sang, J. Hong, K.J. Yoon, J.W. Son, J.H. Lee, B.K. Kim, H. Kim, Catalytic behavior of metal catalysts in high-temperature RWGS reaction: In-situ FT-IR experiments and first-principles calculations, Scientific Reports, 7 (2017) 41207.

[21] D.H. Kim, J.L. Park, E.J. Park, Y.D. Kim, S. Uhm, Dopant Effect of Barium Zirconate-Based Perovskite-Type Catalysts for the Intermediate-Temperature Reverse Water Gas Shift Reaction, Acs Catalysis, 4 (2014) 3117-3122.

[22] A.M. Bahmanpour, F. Héroguel, M. Kl, C.J. Baranowski, O. Krcher, Essential role of oxygen vacancies of Cu-Al and Co-Al spinel oxides in their catalytic activity for the reverse water gas shift reaction, Applied Catalysis B: Environmental, 266 (2020) 118669-118676.

[23] Cu-Al Spinel as a Highly Active and Stable Catalyst for the Reverse Water Gas Shift Reaction, Acs Catalysis, 9 (2019) 6243-6251.

[24] C.J. Keturakis, M. Zhu, E.K. Gibson, M. Daturi, I.E. Wachs, Dynamics of CrO_3-Fe_2O_3 Catalysts during the High-Temperature Water-Gas Shift Reaction: Molecular Structures and Reactivity, ACS Catalysis, 6 (2016) 4786-4798.

[25] X. Zhang, Y. Liu, M. Zhang, T. Yu, B. Chen, Y. Xu, M. Crocker, X. Zhu, Y. Zhu, R. Wang, Synergy between β-Mo_2C Nanorods and Non-thermal Plasma for Selective CO_2 Reduction to CO, 6 (2020) 3312-3328.

[26] D. Vovchok, C. Zhang, S. Hwang, L. Jiao, J.A. Rodriguez, Deciphering Dynamic Structural and Mechanistic Complexity in Cu/CeO_2 /ZSM-5 Catalysts for the Reverse Water-Gas Shift Reaction, ACS Catalysis, 10 (2020) 10216–10228.

[27] Y. Wang, C. Zhang, X. Wang, J. Guo, H. Zhang, Site Selective CO_2 Reduction over Highly Dispersed Ru-SnOx Sites Derived from [Ru@Sn9]6-Zintl Cluster, ACS Catalysis, 10 (2020) 7808-7819.

[28] J.A. Rodriguez, S. Ma, P. Liu, J. Hrbek, J. Evans, M. Pérez, Activity of CeO_x and TiO_x Nanoparticles Grown on Au(111) in the Water-Gas Shift Reaction, Science, 318 (2017) 1757-1760.

[29] G. Jacobs, S. Ricote, P.M. Patterson, U.M. Graham, A. Dozier, S. Khalid, E. Rhodus, B.H. Davis, Low temperature water-gas shift: Examining the efficiency of Au as a promoter for ceria-based catalysts prepared by CVD of a Au precursor, Applied Catalysis A General, 292 (2005) 229-243.

[30] C. L., Wang, and, M., Tahvildar, Khazaneh, and, D., Widmann, and, TAP reactor studies of the oxidizing capability of CO_2 on a Au/CeO_2 catalyst-A first step toward identifying a redox mechanism in the Reverse Water－Gas Shift reaction - ScienceDirect, Journal of Catalysis, 302 (2013) 20-30.

[31] R.J. Madon, D. Braden, S. Kandoi, P. Nagel, M. Mavrikakis, J.A. Dumesic, Microkinetic analysis and mechanism of the water gas shift reaction over copper catalysts, Journal of Catalysis, 281 (2011) 1-11.

[32] C.l. Galván, J. Schumann, M. Behrens, J.L.G. Fierro, E. Frei, Reverse Water-Gas Shift Reaction at the Cu/ZnO interface: Influence of the Cu/Zn ratio on structure-activity correlations, Applied Catalysis B Environmental, 195 (2016) 104-111.

[33] X. Chen, X. Su, H. Duan, B. Liang, Y. Huang, T. Zhang, Catalytic performance of the Pt/TiO_2 catalysts in reverse water gas shift reaction: Controlled product selectivity and a mechanism

study, Catalysis Today, 281 (2017) 312-318.

[34] Cao, Zhaoru, Guo, Ling, Zheng, Xiaoli, Shi, Yayin, Liu, Naying, Theoretical study on the reaction mechanism of reverse water-gas shift reaction using a Rh-Mo6S8 cluster, RSC Advances, 6 (2016) 108270-108279.

[35] N. Habibi, Y. Wang, H. Arandiyan, M. Rezaei, Low-temperature synthesis of mesoporous nanocrystalline magnesium aluminate ($MgAl_2O_4$) spinel with high surface area using a novel modified sol-gel method, Advanced Powder Technology, 28 (2017) 1249-1257.

[36] M. Yang, S. Li, Y. Wang, J.A. Herron, Y. Xu, L.F. Allard, S. Lee, J. Huang, M. Mavrikakis, M. Flytzani-Stephanopoulos, Catalytically active Au-O(OH)x- species stabilized by alkali ions on zeolites and mesoporous oxides, Science, 346 (2014) 1498.

[37] M.M. Millet, G. Algara-Siller, S. Wrabetz, A. Mazheika, F. Girgsdies, D. Teschner, F. Seitz, A. Tarasov, S.V. Leychenko, R. Schloegl, Ni Single Atom Catalysts for CO_2 Activation, Journal of the American Chemical Society, 141 (2019) 2451-2461.

[38] Y. Tang, Y. Wei, Z. Wang, S. Zhang, Y. Li, L. Nguyen, Y. Li, Y. Zhou, W. Shen, F.F. Tao, Synergy of Single-Atom Ni_1 and Ru_1 Sites on CeO_2 for Dry Reforming of CH_4, Journal of the American Chemical Society, 141 (2019) 7283-7293.

[39] A.P. Grosvenor, M.C. Biesinger, R.S.C. Smart, N.S. McIntyre, New interpretations of XPS spectra of nickel metal and oxides, Surface Science, 600 (2006) 1771-1779.

[40] T.D. Nguyen-Phan, S. Luo, Z.Liu, et al, Striving Toward Noble-Metal-Free Photocatalytic Water Splitting: The Hydrogenated-Graphene-TiO_2 Prototype, Chemistry of Materials, 27 (2015) 6282-6296.

[41] J.C. Dupin, D. Gonbeau, P. Vinatier, A. Levasseur, Systematic XPS studies of metal oxides, hydroxides and peroxides, Physical Chemistry Chemical Physics, 2 (2000) 1319-1324.

[42] X. Su, X. Yang, B. Zhao, Y. Huang, Designing of highly selective and high-temperature endurable RWGS heterogeneous catalysts: recent advances and the future directions, Journal of Energy Chemistry, (2017) 854-867.

[43] J. Szanyi, J.H. Kwak, Dissecting the steps of CO_2 reduction: 1. The interaction of CO and CO_2 with γ-Al_2O_3: an in situ FTIR study, Physical Chemistry Chemical Physics, 16 (2014) 15117-15125.

[44] G. Jacobs, B.H. Davis, Reverse water-gas shift reaction: steady state isotope switching study of the reverse water-gas shift reaction using in situ DRIFTS and a Pt/ceria catalyst, Applied Catalysis A General, 284 (2005) 31-38.

[45] J.M. Trillo, G. Munuera, J.M. Criado, Catalytic Decomposition of Formic Acid on Metal Oxides, Catalysis Reviews, 7 (1972) 51-86.

[46] X. Wang, H. Shi, J. Kwak, J. Szanyi, Mechanism of CO_2 Hydrogenation on Pd/Al_2O_3 Catalysts: Kinetics and Transient DRIFTS-MS Studies, Acs Catalysis, 5 (2015) 6337–6349.

[47] D. Vovchok, C. Zhang, S. Hwang, L. Jiao, J.A. Rodriguez, Deciphering Dynamic Structural and Mechanistic Complexity in Cu/CeO_2 /ZSM-5 Catalysts for the Reverse Water-Gas Shift Reaction, ACS Catalysis, 10 (2020) 10216-10228.